

Non-Hermitian Floquet topological phases with arbitrarily many real-quasienergy edge states

Longwen Zhou^{1,2,*} and Jiangbin Gong^{1,†}

¹*Department of Physics, National University of Singapore, Singapore 117551, Republic of Singapore*

²*Department of Physics, College of Information Science and Engineering, Ocean University of China, Qingdao 266100, China*

(Dated: 2018-11-27)

Topological states of matter in non-Hermitian systems have attracted a lot of attention due to their intriguing dynamical and transport properties. In this study, we propose a periodically driven non-Hermitian lattice model in one-dimension, which features rich Floquet topological phases. The topological phase diagram of the model is derived analytically. Each of its non-Hermitian Floquet topological phases is characterized by a pair of integer winding numbers, counting the number of *real* 0- and π -quasienergy edge states at the boundaries of the lattice. Non-Hermiticity induced Floquet topological phases with unlimited winding numbers are found, which allow arbitrarily many *real* 0- and π -quasienergy edge states to appear in the complex quasienergy bulk gaps in a well-controlled manner. We further suggest to probe the topological winding numbers of the system by dynamically imaging the stroboscopic spin textures of its bulk states.

I. INTRODUCTION

Floquet topological states of matter appear in systems described by time-periodic Hamiltonians. Being intrinsically out-of-equilibrium, these states are characterized by topological invariants, bulk-edge relations and classification schemes that are either similar to or distinct from their static counterparts [1–31]. Under properly designed driving fields, Floquet topological phases with many edge states can be engineered [6–9, 32], resulting in intriguing transport signatures [33, 34]. Especially, recipes and prototypical models were discovered, which allow the generation of unlimited number of degenerate $0/\pi$ edge modes [35, 36], chiral edge states [37] and linked nodal loops [38] in well-controlled manners. Experimentally, Floquet topological states have also been found in cold atom, photonic, phononic and acoustic systems [39–45].

In more general situations, the physical setups used to realize Floquet topological phases are usually subject to gain and loss or environment-induced dissipations [46]. These processes could be effectively described by introducing a non-Hermitian part to the Hamiltonian of the Floquet system. The dynamics of the system, now induced effectively by a time-periodic non-Hermitian Hamiltonian would then be non-unitary, and the quasienergies of the corresponding Floquet operator (i.e., time evolution operator over a complete driving period) could also be complex. How will these non-Hermitian effects change a Floquet topological state, and whether non-Hermiticity induced Floquet topological phases with new features could appear in these systems are largely unexplored [47, 48]. In some previous studies, periodic drivings have been employed to stabilize stroboscopic dynamics [49] and reveal signatures of exceptional points (EPs) [51–57]. In another early work, losses have been introduced as dissipative probes to the topological invariants of a Hermitian lattice model [58]. This idea motivates further theoretical analysis and experimental realizations of non-Hermitian

quantum walks [59–65], together with the detection of their topological invariants [66].

In this manuscript, we further reveal the richness of Floquet topological phases in non-Hermitian systems. We first propose a periodically driven non-Hermitian lattice model, which could be realizable in various types of quantum simulators. Under periodic boundary conditions (PBC), the phase diagram of the model is obtained by deriving the general conditions for band touching points (BTPs) to appear in its complex Floquet quasienergy spectrum. Each of the phases is further shown to be characterized by a pair of integer topological winding numbers. Under open boundary conditions (OBC), these winding numbers predict the number of topological edge states appear at zero and π -quasienergies in the Floquet spectrum. Remarkably, our simple model shows that it is possible to have a non-Hermitian Floquet system with unlimited winding numbers and arbitrarily many topological edge states with *purely real* quasienergies. Finally, we propose to image the stroboscopic spin textures of our system, whose patterns have direct connections with the winding numbers of each of its non-Hermitian Floquet topological phases.

II. THE MODEL

In this study, we focus on a tight-binding lattice model with a ladder geometry, which is subjected to piecewise time-periodic quenches. The geometry of the lattice is illustrated in Fig. 1, with two sublattices A and B in each of its unit cells. The time-dependent Hamiltonian of the lattice is given by:

$$\hat{H}(t) = \begin{cases} \hat{H}_1, & t \in \left[\ell T, \ell T + \frac{T}{2} \right). \\ \hat{H}_2, & t \in \left[\ell T + \frac{T}{2}, \ell T + T \right). \end{cases} \quad (1)$$

Here $\hat{H}_1 = \sum_n [ir_y(|n+1\rangle\langle n| - \text{h.c.}) + 2i\gamma|n\rangle\langle n|] \otimes \sigma_y$, $\hat{H}_2 = \sum_n [r_x(|n\rangle\langle n+1| + \text{h.c.}) + 2\mu|n\rangle\langle n|] \otimes \sigma_x$, $\ell \in \mathbb{Z}$, T is the driving period, $n \in \mathbb{Z}$ is the unit cell index and the lattice constant has been set to 1. The system parameters r_x, r_y, μ and γ all take real values. The Pauli matrices σ_x, σ_y act on sublattice degrees of freedom A and B.

In the first half of a driving period, the lattice Hamiltonian

* zhoulw13@u.nus.edu

† phygj@nus.edu.sg

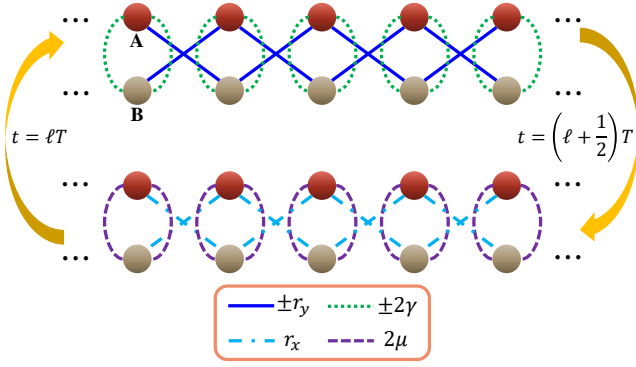


FIG. 1. A sketch to the geometry of the periodically driven non-Hermitian lattice model Eq. (1) over a complete driving period. Each of the unit cells contains two sublattices A and B. In the first half of the driving period, the system has non-Hermitian intracell couplings $\pm 2\gamma$ and intercell couplings $\pm r_y$ among adjacent unit cells. In the second half of the driving period, the system has intracell couplings 2μ and intercell couplings r_x among adjacent unit cells. The same sequence of quenches repeat in each driving period.

contains intercell hoppings $\pm r_y$ between A, B sublattices in nearest neighbor unit cells, and asymmetric couplings $\pm 2\gamma$ between sublattices A, B in the same unit cell, which introduce non-Hermitian effects. In experimental setups like coupled-resonator waveguides, such asymmetric couplings may be realized by the asymmetric scattering between a clockwise and a counterclockwise propagating mode within each resonator [67]. These two resonator modes correspond to the A, B sublattices. Their internal coupling can be made asymmetric by opening the system, resulting in asymmetric internal scattering and losses within the cavity. In alternative experimental setups like cold atoms in optical lattices, the A, B sublattices are replaced by spins of cold atoms. Under a simple rotation $\sigma_y \rightarrow \sigma_z$ yielding a mathematically equivalent model, the non-Hermitian term becomes $i\gamma\sigma_z$, which is associated with particle gain/loss for spin up/down atoms (assuming $\gamma > 0$). Experimentally, it may be realized by introducing an atom loss of strength $-2i\gamma$ for spin down atoms only, which could be generated using a resonant optical beam to kick the atoms in the spin-down state out of a trap. One may also consider applying a radio frequency pulse to excite atoms in the spin-down state to another irrelevant state, leading to an effective decay when atoms in that state experience a loss by applying an antitrap [68].

In the second half of a driving period, the lattice Hamiltonian is Hermitian, with hoppings 2μ and r_x between sublattices A and B in the same unit cell and among nearest neighbor unit cells, respectively. This relatively simple lattice model should also be realizable in both coupled resonator and cold atom systems. Putting together, the Floquet operator describing the evolution of the system over a complete driving period is given by

$$\hat{U} = e^{-i\sum_n \left[\frac{\sigma_z}{2} (n)\langle n+1 | + \text{h.c.} \right] + \mu |n\rangle\langle n|} \otimes \sigma_x \times e^{-i\sum_n \left[\frac{\sigma_z}{2} (n)\langle n+1 | - \text{h.c.} \right] + i\gamma |n\rangle\langle n|} \otimes \sigma_y, \quad (2)$$

where we have set $\hbar = T = 1$ and chosen \hbar/T to be the unit of energy. Under PBC, the Floquet operator \hat{U} can also be expressed in momentum representation as $\hat{U} = \sum_k U(k)|k\rangle\langle k|$, where

$$U(k) = e^{-ih_x(k)\sigma_x} e^{-i[h_y(k)+i\gamma]\sigma_y}, \quad (3)$$

$$h_x(k) = \mu + r_x \cos(k), \quad (4)$$

$$h_y(k) = r_y \sin(k), \quad (5)$$

and $k \in [-\pi, \pi)$ is the quasimomentum. Without periodic drivings, topological phases in similar non-Hermitian lattice models have been explored in several studies [69–78]. In the following, we will show that the periodic quenches considered in this manuscript make the system much richer in realizing non-Hermitian topological states with real quasienergies, with the possibility of reaching phases with arbitrarily large topological invariants and induced solely by non-Hermitian effects.

III. BULK PROPERTIES

To reveal the richness of Floquet topological phases in the periodically driven non-Hermitian lattice (PDNHL) model introduced in Eq. (1), we first analyze the bulk quasienergy spectrum and eigenstates of its Floquet operator $U(k)$ in the following subsections. By investigating the gapless condition of the quasienergy spectrum, we obtain the trajectories of Floquet BTPs in the parameter space, which form the boundaries of different non-Hermitian Floquet topological phases. We further introduce a pair of integer winding numbers, which could uniquely characterize each of the Floquet topological phases in the phase diagram.

A. Floquet spectrum and band-touching points

The Floquet spectrum of $U(k)$ as defined in Eq. (3) has two quasienergy bands $\pm E(k)$ [79], with $E(k)$ being an eigenvalue of the effective Floquet Hamiltonian $H(k) = -i \ln U(k)$. Since $H(k)$ is non-Hermitian, we in general have $E(k) \neq E^*(k)$. But similar to Hermitian Floquet systems, the real part of $E(k)$ is a phase factor, which is defined modulus 2π and take values in the first quasienergy Brillouin zone $(-\pi, \pi]$. Therefore the Floquet spectrum of $U(k)$ could have two gaps around $E(k) = 0$ and $E(k) = \pi$ in the complex quasienergy plane.

Combining the two parts of quenches in Eq. (3), $U(k)$ can be written as $U(k) = e^{-iE(k)\hat{\mathbf{n}}\cdot\boldsymbol{\sigma}}$, where $\hat{\mathbf{n}}$ is a unit vector and $\boldsymbol{\sigma} = (\sigma_x, \sigma_y, \sigma_z)$. Then using the formula $e^{i\theta\hat{\mathbf{n}}\cdot\boldsymbol{\sigma}} = \cos(\theta) + i\sin(\theta)\hat{\mathbf{n}}\cdot\boldsymbol{\sigma}$ to Eq. (3), it is not hard to see that $E(k)$ satisfies the equation:

$$\cos[E(k)] = \cos[h_x(k)] \cos[h_y(k) + i\gamma]. \quad (6)$$

Then if the quasienergy gap closes at $E(k) = 0$ or $E(k) = \pi$, we will have $\cos[E(k)] = 1$ or $\cos[E(k)] = -1$, respectively. Plugging Eqs. (4) and (5) into the right hand side of Eq. (6), we find the gapless conditions to be $\mu + r_x \cos(k) = m\pi \pm \arccos\left[\frac{1}{\cosh(\gamma)}\right]$ and $r_y \sin(k) = n\pi$, where m, n are integers of

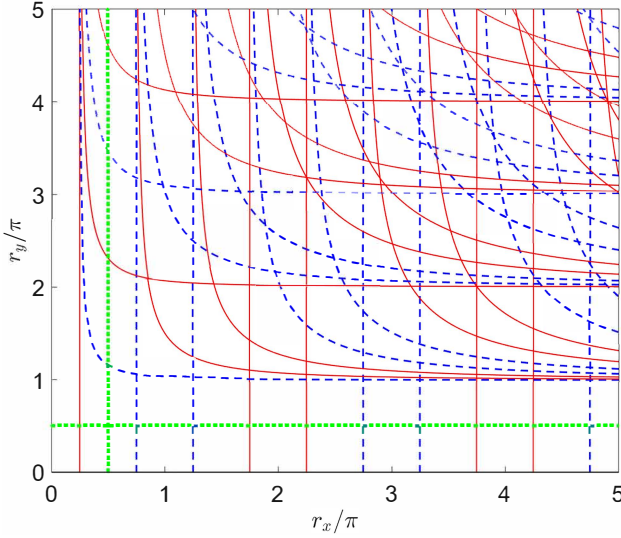


FIG. 2. Phase boundary diagram of the PDNHL model in the parameter space $(r_x, r_y) \in (0, 5\pi) \times (0, 5\pi]$, with other system parameters fixed at $\mu = 0$ and $\gamma = \text{arccosh}(\sqrt{2})$. Trajectories of Floquet BTPs corresponding to spectrum gap closings at quasienergy zero (π) are denoted by red solid (blue dashed) lines, separating potentially different non-Hermitian Floquet topological phases. Green dotted lines represent parameter sets in which the topological properties of the system are further explored in later sections.

the same parity (opposite parities) if the gap closes at $E(k) = 0$ [$E(k) = \pi$]. Combining these gapless conditions together with the help of the identity $\cos^2(k) + \sin^2(k) = 1$, we find the equation for trajectories of Floquet BTPs (i.e., BTPs of the complex quasienergy spectrum) in the parameter space as:

$$\frac{1}{r_x^2} \left\{ m\pi \pm \arccos \left[\frac{1}{\cosh(\gamma)} \right] - \mu \right\}^2 + \frac{n^2 \pi^2}{r_y^2} = 1, \quad (7)$$

where $m, n \in \mathbb{Z}$. These trajectories form boundaries separating different non-Hermitian Floquet topological phases, as will be discussed in the following subsections.

B. Phase boundaries

Before presenting explicit examples of the phase diagram at finite values of the non-Hermitian coupling strength γ , let's first discuss two limiting cases. In the Hermitian limit ($\gamma = 0$), Eq. (7) reduces to $\frac{(m\pi - \mu)^2}{r_x^2} + \frac{n^2 \pi^2}{r_y^2} = 1$. The topological phases in the corresponding Hermitian Floquet system have been explored in Ref. [36], with very rich Floquet topological states identified theoretically in the context of a spin-1/2 kicked rotor. In the opposite limit ($\gamma \rightarrow \infty$), Eq. (7) is simplified to $\frac{(m\pi \pm \frac{\pi}{2} - \mu)^2}{r_x^2} + \frac{n^2 \pi^2}{r_y^2} = 1$. In this case, Floquet BTPs appearing at zero and π quasienergies tend to coincide with each other in the parameter space, resulting in simpler phase boundary structures. For completeness, we present examples of phase boundary diagrams near these two limits in the Appendix A.

For a general non-Hermitian coupling $\gamma \neq 0$, the phase boundaries (gap-closing lines) separating potentially different topological phases are splitted and deformed from the Hermitian limit by an amount $\sim \pm \arccos \left[\frac{1}{\cosh(\gamma)} \right]$. Note that these changes cannot be eliminated by tuning the strength of intra-cell hopping μ , which indicates their genuine non-Hermitian origin. In Fig. 2, we present an example of the phase boundary diagram (formed by gap-closing lines in the r_x - r_y parameter space) with $\mu = 0$ at a fixed $\gamma = \text{arccosh}(\sqrt{2})$. Floquet BTPs forming the red solid (blue dashed) lines are related to spectrum gap closings at quasienergy zero (π), separating potentially different non-Hermitian Floquet topological phases. We further notice that for any given integers m and n , the Floquet BTPs related to the two branches $\pm \arccos \left[\frac{1}{\cosh(\gamma)} \right]$ of phase boundaries are always due to gap closings at the same quasienergy (either zero or π). In between these two branches, new Floquet topological phases that are absent in the Hermitian limit may emerge. In the next subsection, we will give a unique characterization of the phase formed in each closed patch on the phase boundary diagram through a pair of topological invariants.

C. Topological winding number and phase diagram

The symmetry classification of Hermitian Floquet topological states has been established in several studies [30, 31]. In one dimension, all Floquet topological states in Hermitian systems are symmetry protected. One important class of these topological phases is that protected by a chiral symmetry. Each one-dimensional Floquet topological phase with chiral symmetry is characterized by a pair of integer winding numbers, defined in two symmetric time frames of the system's Floquet operator [28]. For non-Hermitian Floquet systems, however, a general symmetry classification scheme has not yet been formulated. Our study here provides useful resources for the establishment of such a framework.

The Floquet operator $U(k)$ of our PDNHL model in Eq. (3) has chiral symmetry in two symmetric time frames. These frames are obtained by shifting the starting time of the evolution forward or backward over half of the driving period. The resulting Floquet operators in these symmetric time frames are given by:

$$U_1(k) = e^{-i\frac{h_x(k)}{2}\sigma_x} e^{-i[h_y(k)+i\gamma]\sigma_y} e^{-i\frac{h_x(k)}{2}\sigma_x}, \quad (8)$$

$$U_2(k) = e^{-i\frac{h_y(k)+i\gamma}{2}\sigma_y} e^{-ih_x(k)\sigma_x} e^{-i\frac{h_y(k)+i\gamma}{2}\sigma_y}. \quad (9)$$

Note that $U_1(k)$ and $U_2(k)$ are differ from $U(k)$ by similarity transformations, and therefore sharing with it the same complex quasienergy spectrum. However, these Floquet operators in different time frames are not unitarily equivalent due to the non-Hermiticity of our system. The chiral symmetry of $U_1(k)$ and $U_2(k)$ is described by a unitary transformation $\Gamma = \Gamma^\dagger = \Gamma^{-1}$, under which

$$\Gamma U_\alpha(k) \Gamma = U_\alpha^{-1}(k), \quad \alpha = 1, 2. \quad (10)$$

It is not hard to see that $\Gamma = \sigma_z$ satisfies this condition, and therefore describes the chiral symmetry of our PDNHL model.

With the chiral symmetry, we can introduce winding numbers for $U_1(k)$ and $U_2(k)$ following the same routine as in Hermitian Floquet systems [28]. Using the Euler formula and Eq. (6), we can rewrite $U_1(k)$ and $U_2(k)$ as

$$U_\alpha(k) = \cos[E(k)] - i[n_{\alpha x}(k)\sigma_x + n_{\alpha y}(k)\sigma_y], \quad (11)$$

where $\alpha = 1, 2$, and the components $n_{\alpha x}(k)$ and $n_{\alpha y}(k)$ are given by:

$$n_{1x}(k) = \sin[h_x(k)] \cos[h_y(k) + i\gamma], \quad (12)$$

$$n_{1y}(k) = \sin[h_y(k) + i\gamma], \quad (13)$$

$$n_{2x}(k) = \sin[h_x(k)], \quad (14)$$

$$n_{2y}(k) = \cos[h_x(k)] \sin[h_y(k) + i\gamma]. \quad (15)$$

Notably, due to the chiral symmetry, both the real and imaginary parts of vectors $\mathbf{n}_1(k) = [n_{1x}(k), n_{1y}(k)]$ and $\mathbf{n}_2(k) = [n_{2x}(k), n_{2y}(k)]$ are constrained to move in a two dimensional plane under the change of k . Therefore they have well defined winding numbers around the origin of the plane, given by

$$W_\alpha = \int_{-\pi}^{\pi} \frac{dk}{2\pi} \frac{n_{\alpha x}(k)\partial_k n_{\alpha y}(k) - n_{\alpha y}(k)\partial_k n_{\alpha x}(k)}{n_{\alpha x}^2(k) + n_{\alpha y}^2(k)} \quad (16)$$

for $\alpha = 1, 2$. Even though the integrand of these winding numbers have non-vanishing imaginary parts, it has been shown that these imaginary parts in general have no windings under the integral of quasimomentum k over the first Brillouin zone [74]. Therefore both W_1 and W_2 are real and take integer values. Combining these winding numbers allows us to introduce another pair of winding numbers W_0 and W_π , defined as

$$W_0 = \frac{W_1 + W_2}{2}, \quad W_\pi = \frac{W_1 - W_2}{2}. \quad (17)$$

These winding numbers will be used to characterize the non-Hermitian Floquet topological phases of our system.

As an example, we present in Fig. 3 the calculations of W_0 (blue circles) and W_π (red stars) along two trajectories (dotted lines) in the phase boundary diagram Fig. 2. We see that in both cases, the winding numbers only take integer values, as suggested by our theory. Furthermore, the value of W_0 (W_π) has a quantized jump every time when a trajectory of Floquet BTPs related to gap closings at quasienergy zero (π) is crossed in the parameter space. These observations indicate that the trajectories of Floquet BTPs described by Eq. (7) are indeed boundaries of different non-Hermitian Floquet topological phases characterized by different values of winding numbers (W_0, W_π). Comparing Fig. 3(a) with the phase diagram Fig. 1 reported in Ref. [36], which studied the Floquet topological phases of our model in its Hermitian limit, we also find new topological phases in the range of system parameters $n\pi - \arccos\left[\frac{1}{\cosh(\gamma)}\right] < r_x < n\pi + \arccos\left[\frac{1}{\cosh(\gamma)}\right]$ for all $n \in \mathbb{Z}$, which are solely induced by non-Hermitian effects ($\gamma \neq 0$). Furthermore, these non-Hermiticity induced Flo-

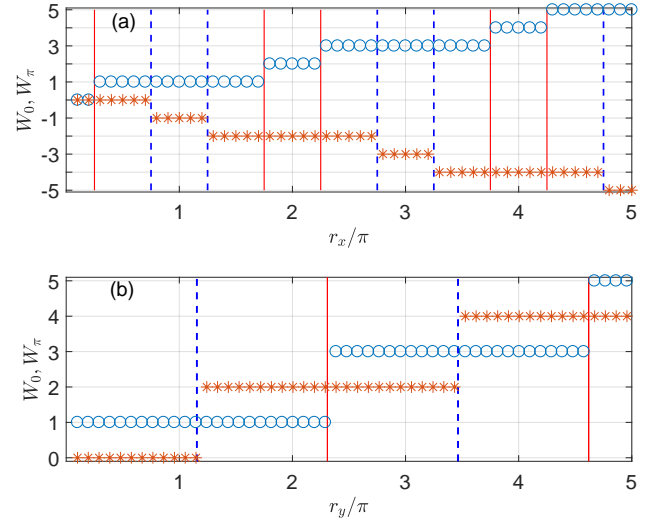


FIG. 3. Winding numbers W_0 (circles) and W_π (stars) versus system parameters r_x [in panel (a)] and r_y [in panel (b)], calculated along the two green dotted lines in the phase boundary Fig. 2. Red solid (blue dashed) lines denote phase boundaries mediated by spectrum gap closings at quasienergy zero (π), which are obtained by solving Eq. (7) under the condition $n = 0$ ($m = 0$).

quet topological phases could possess arbitrarily large winding numbers. For example, in the range of parameters $r_x \in (n\pi - \arccos\left[\frac{1}{\cosh(\gamma)}\right], n\pi + \arccos\left[\frac{1}{\cosh(\gamma)}\right])$, $r_y \in (0, \pi)$ and for any $\gamma \in (0, \infty)$, we have $(W_0, W_\pi) = (n, -n)$ for any $n \in \mathbb{Z}^+$.

To demonstrate the later point, we present in Fig. 4 the calculation of (W_0, W_π) as defined in Eq. (17) versus the hopping amplitude r_x , with other system parameters fixed at $\mu = 0$, $r_y = \frac{\pi}{2}$ and $\gamma = \text{arccosh}(\sqrt{2})$. The linear and unbounded growth of W_0 and W_π are clearly seen with the increase of r_x . Note that the non-Hermitian topological phases appearing in the region $r_x \in (n\pi - \arccos\left[\frac{1}{\cosh(\gamma)}\right], n\pi + \arccos\left[\frac{1}{\cosh(\gamma)}\right])$ for any $n \in \mathbb{Z}$ are absent in the Hermitian limit ($\gamma = 0$) of the system.

To give a more global view of the topological phases that can appear in our system, we show in Fig. 5 the results of W_0 and W_π in the range of system parameters $(r_x, r_y) \in [0, 3\pi] \times [0, 3\pi]$, with $\mu = 0$ and the non-Hermitian coupling strength $\gamma = \text{arccosh}(\sqrt{2})$. In panels 5(a) and 5(b), each color corresponds to a range of system parameters (r_x, r_y) in which W_0 or W_π takes the same value, as also specified in the figure. The trajectories of Floquet BTPs corresponding to gap closings at quasienergies zero (solid lines) and π (dashed lines) are also denoted in the figure. They are found to match precisely the boundaries across which the values of W_0 or W_π take quantized changes. Therefore we conclude that the trajectories of Floquet BTPs in the parameter space, as predicted by Eq. (7), are indeed boundaries of different non-Hermitian Floquet topological phases characterized by different values of winding numbers (W_0, W_π).

The next question to ask concerns the physical implication of these winding numbers. In the following two sections, we try to address this issue from two complementary perspec-

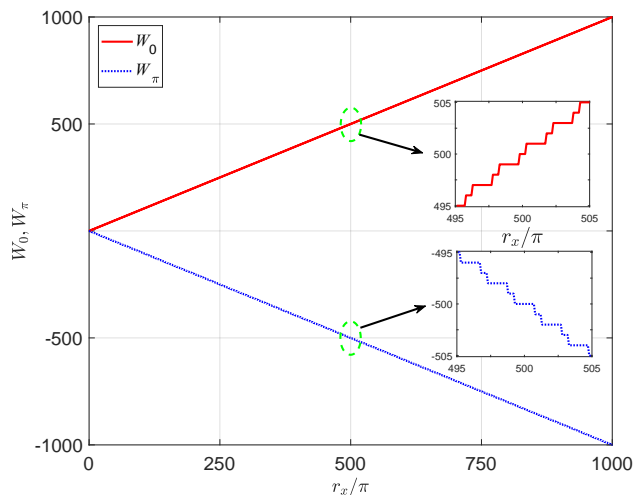


FIG. 4. The linear growth of winding numbers W_0 (red solid line) and W_π (blue dotted line) versus system parameters r_x , with other system parameters fixed at $\mu = 0$, $r_y = \frac{\pi}{2}$ and $\gamma = \text{arccosh}(\sqrt{2})$. Green dashed circles highlight the regions in which zoomed in results of W_0 and W_π are shown in internal panels.

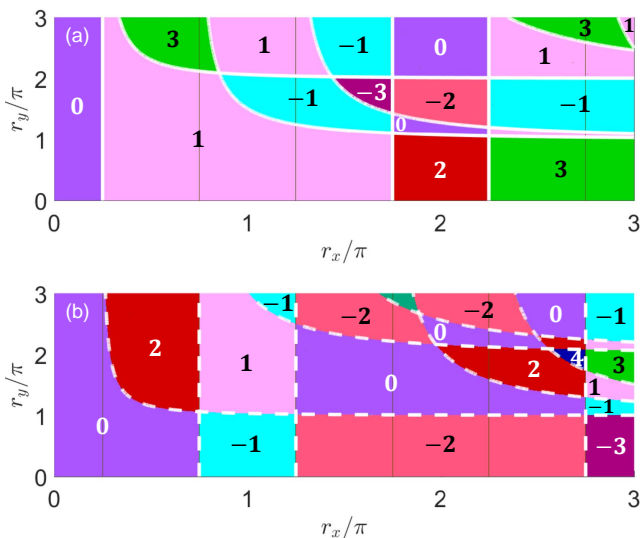


FIG. 5. Winding numbers W_0 [panel (a)] and W_π [panel (b)] in the range of system parameters $(r_x, r_y) \in (0, 3\pi) \times (0, 3\pi)$, with other parameters fixed at $\mu = 0$ and $\gamma = \text{arccosh}(\sqrt{2})$. In panel (a)\(b), regions with the same color share the same values of W_0 \(W_π), as also denoted by the integers in the panels. The white solid\dashed lines in panel (a)\(b) are trajectories of Floquet BTPs obtained from Eq. (7) and related to gap closings at quasienergy 0 \(π). They match precisely with the topological phase boundaries at which W_0 or W_π gets quantized jumps.

tives: the edge states and bulk dynamics.

IV. EDGE STATES

In one dimensional chiral symmetric Hermitian Floquet systems, the winding numbers W_0 and W_π have a direct connection with the number of degenerate edge state pairs n_0 and n_π at quasienergies zero and π [28], i.e.,

$$n_0 = |W_0|, \quad n_\pi = |W_\pi|. \quad (18)$$

This relation belongs to the family of bulk-edge correspondence in topological insulators. Experimentally, it also provides a useful route to detect topological invariants of bulk materials through quantized transport along their boundaries, and to distinguish topologically distinct states of matter by imagining bound states appearing at their interfaces.

In non-Hermitian systems, however, the relation between bulk invariants and edge states becomes a subtle issue due to the existence of EPs, which could make the Hamiltonian matrix of the system defective (algebraic multiplicity \neq geometric multiplicity), with its spectrum extremely sensitive to boundary conditions [46]. Cases regarding the breakdown of bulk-edge correspondence and its reparation in non-Hermitian systems have been explored in several studies [69, 73, 74, 77, 78, 80–85], with still unsettled debates over the literature. The PDNHL model we introduced in Eq. (1) provides an example, in which the bulk-edge relation (18) for Hermitian Floquet systems still holds, with all topological edge states taking real quasienergies

To show this, we studied the quasienergy spectrum and edge states of Floquet operator \hat{U} as defined in Eq. (2). Numerically, they are obtained by solving the eigenvalue equation $\hat{U}|\psi\rangle = e^{-iE}|\psi\rangle$ under OBC. As an example, we presented in Fig. 6 the Floquet spectrum E versus hopping amplitude r_x at fixed values of hopping amplitude $r_y = \frac{\pi}{2}$ and non-Hermitian coupling strength $\gamma = \text{arccosh}(\sqrt{2})$ in a lattice of $N = 150$ unit cells. In Fig. 6(c), the red solid and blue dashed lines correspond to phase boundaries obtained from the Eq. (7) for Floquet BTPs. We see that the number of edge state pairs (n_0, n_π) , as denoted in Fig. 6(c), changes across each of the phase boundaries. Furthermore, refer to Fig. 5, we find that (n_0, n_π) matches exactly the absolute values of winding number $(|W_0|, |W_\pi|)$ in each of the corresponding non-Hermitian Floquet topological phases. Therefore the relation (18) is verified for the example considered here. With the increase of r_x , the bulk-edge relation (18) and unlimited winding numbers as shown in Fig. 4 then allow arbitrarily many zero and π topological edge states to appear with purely real quasienergies. This gives the first example of generating many topological edge states in non-Hermitian systems following the Floquet engineering approach.

In Appendix B, we present an example of the quasienergy spectrum E versus r_y , for which the bulk-edge relation (18) again survives the test. In more general situations (e.g., along the direction $r_x = r_y$ in Fig. 2), the verification of Eq. (18) in our PDNHL is more demanding due to the complicated configuration of BTPs in the phase diagram, which can result in many topological phase transitions and fluctuations of the edge state numbers in a relatively small parameter window. A

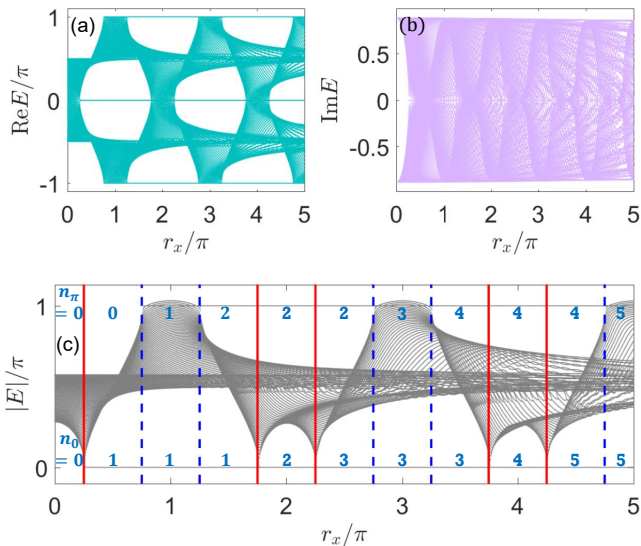


FIG. 6. The Floquet spectrum of \hat{U} versus hopping amplitude r_x under OBC. The lattice has $N = 150$ unit cells. Other system parameters are fixed at $\mu = 0$, $r_y = \frac{\pi}{2}$ and $\gamma = \text{arccosh}(\sqrt{2})$. Panels (a) and (b) show the real and imaginary parts of the quasienergy E . Panel (c) shows the absolute values of quasienergy E . Red solid (blue dashed) lines represent phase boundaries at which the spectrum gap close at quasienergy zero (π). They are obtained from Eq. (7) for Floquet BTPs. The integers in light blue in panel (c) denote the number of degenerate edge state pairs at quasienergies zero (n_0) and π (n_π). Their values are equal to the absolute values of winding numbers W_0 and W_π as shown in Fig. 3(a), respectively.

more systematic understanding of these situations may require statistical-type treatments, and will be left for future studies.

Note in passing that in certain regions of the Floquet spectrum (e.g. $\pi - \arccos\left[\frac{1}{\cosh(\gamma)}\right] < r_x < 1 + \arccos\left[\frac{1}{\cosh(\gamma)}\right]$) of Fig. 6), it seems that there are no bulk quasienergy gaps at $E = \pm\pi$. But on the complex quasienergy plane $\text{Re}E\text{-Im}E$, the edge states at $E = \pm\pi$ are still surrounded by complex spectrum gaps. To further clarify this point, we show the quasienergy spectrum at $r_y = \frac{\pi}{2}$, $\gamma = \text{arccosh}(\sqrt{2})$ with $r_x = \frac{\pi}{2}, \pi, \frac{3\pi}{2}$ and 2π in Fig. 7. In all these examples, we see that edge states at $E = 0$ and $\pm\pi$ indeed have real quasienergies and surrounded by gaps in the complex quasienergy plane. The survival of these real-quasienergy edge states in the vicinity of a dissipative bulk may have further applications in achieving robust state manipulations against environmental effects.

V. STROBOSCOPIC SPIN TEXTURES

Besides employing edge states and bulk-edge correspondence, it is also helpful to find a direct probe to the topological winding numbers of our PDNHL model. In this section, we suggest to achieve this by imaging the stroboscopic spin textures of the system in its dynamics following a sudden quench. The detections of these spin textures are already available in certain quantum simulators like ultracold atoms [86]. Our approach is based on an earlier proposal regarding the dynamical

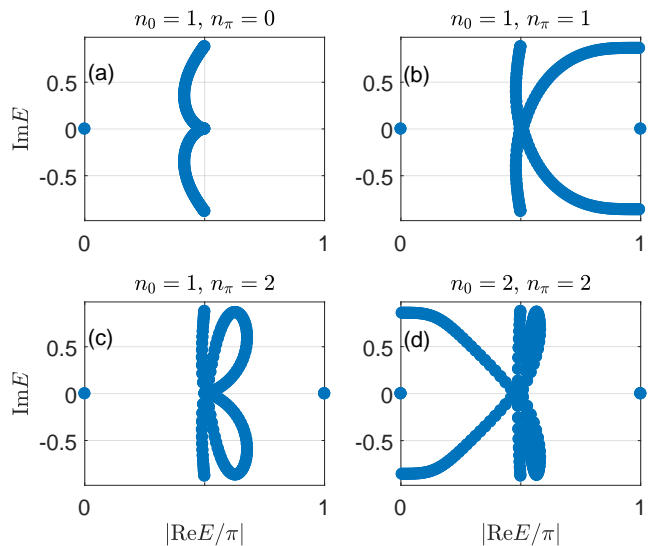


FIG. 7. The Floquet spectrum of \hat{U} at separate values of r_x shown in the complex quasienergy plane. The lattice has $N = 150$ unit cells. Other system parameters are fixed at $\mu = 0$, $r_y = \frac{\pi}{2}$ and $\gamma = \text{arccosh}(\sqrt{2})$. Dots at $\text{Im}E = 0$ and $|\text{Re}E| = 0$ ($|\text{Re}E| = \pi$) represent degenerate edge states with real quasienergy zero (π). Other dots denote bulk states with complex quasienergies. Panel (a): $r_x = \frac{\pi}{2}$, there is one pair of edge states at quasienergy $E = 0$, and no edge states at quasienergy $E = \pi$. Panel (b): $r_x = \pi$, there is one pair of edge states at quasienergy $E = 0$, and one pair of edge states at quasienergy $E = \pi$. Panel (c): $r_x = \frac{3\pi}{2}$, there is one pair of edge states at quasienergy $E = 0$, and two pairs of edge states at quasienergy $E = \pi$. Panel (d): $r_x = 2\pi$, there are two pairs of edge states at quasienergy $E = 0$, and two pairs of states at quasienergy $E = \pi$.

cal classification of topological states [87]. Even though the rigorous proof of the applicability of this proposal to general non-unitary processes has not been fully established, our results strongly indicate that it works at least for our PDNHL model after proper modifications.

In Ref. [87], a dynamical classification of topological quantum phases was introduced following a series of three statements: (i) the classification of a generic d -dimensional gapped topological phase characterized by integer invariants can be reduced to $(d - 1)$ -dimensional invariants defined on something called band inversion surfaces (BISs); (ii) the time-averaged spin-polarizations vanish on BISs in the evolution following a quench from a trivial to a topological phase; (iii) the bulk topological property of the post-quench phase is classified by a dynamical topological invariant determined via a dynamical spin-texture field on BISs.

Let's first elaborate a bit more on the meaning of BISs. According to Ref. [87], the BISs have a static and a dynamical definition. The static definition comes from the following observations. The minimal model of a d -dimensional topological insulator is described by a Bloch Hamiltonian $H(\mathbf{k}) = \sum_{i=1}^{d+1} h_i(\mathbf{k})\gamma_i$. Here γ_i are Pauli matrices for $d = 1, 2$ and Dirac γ matrices for $d = 3, 4$. Ref. [87] suggests to pick out one component, e.g., $h_{d+1}(\mathbf{k})$ from the vector field $\mathbf{h}(\mathbf{k}) = [h_1(\mathbf{k}), \dots, h_d(\mathbf{k}), h_{d+1}(\mathbf{k})]$, and referring to the remain-

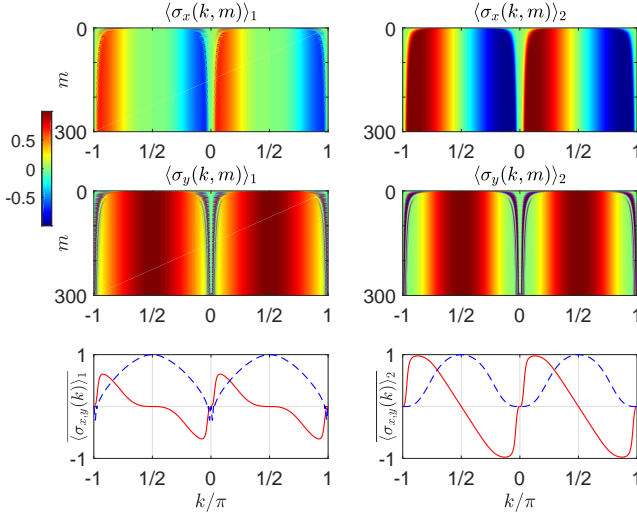


FIG. 8. Stroboscopic spin expectation values $\langle \sigma_j(k, m) \rangle_\alpha$ (top and middle panels) and stroboscopic time-averaged spin textures $\overline{\langle \sigma_j(k) \rangle}_\alpha$ (bottom panels) versus the quasimomentum k for spin components $j = x, y$ in time frames $\alpha = 1, 2$. System parameters are chosen as $\mu = 0$, $r_x = r_y = \frac{\pi}{2}$, and $\gamma = \text{arccosh}(\sqrt{2})$. In bottom panels, results for $\overline{\langle \sigma_x(k) \rangle}_{1,2}$ (red solid lines) and $\overline{\langle \sigma_y(k) \rangle}_{1,2}$ (blue dashed lines) at each k are obtained after averaging over 300 driving periods.

ing components $\mathbf{h}_{\text{SO}} = [h_1(\mathbf{k}), \dots, h_d(\mathbf{k})]$ as a spin-orbit (SO) field. Then the BISs refer to the $(d-1)$ -dimensional surface formed by the collection of all quasimomenta in the first Brillouin zone at which $h_{d+1}(\mathbf{k}) = 0$. For a 1-dimensional model, the BISs are formed by discrete k -points in the first Brillouin zone, which may also be called ‘‘band inversion points’’. On the BISs, a nonzero SO field $h_{\text{SO}}(\mathbf{k})$ then serves as a gap-opening perturbation. Note that according to this definition, the locations and shapes of BISs depend on the choice of $h_{d+1}(\mathbf{k})$, and are therefore not uniquely defined [87]. As will be discussed later, this nonuniqueness is not an issue, as the topological invariant of the system is solely determined by how a spin texture field (to be defined later) changes across the BISs, not the exact locations and shapes of the BISs themselves. This also provides more room for one to choose $h_{d+1}(\mathbf{k})$ conveniently in experiments without affecting the final detection of topological invariants.

This static definition, however, is *not* the definition of BISs we are going to use. This is because for a non-Hermitian Hamiltonian (or Floquet effective Hamiltonian) $H(\mathbf{k})$, $h_{d+1}(\mathbf{k})$ and the SO field $h_{\text{SO}}(\mathbf{k})$ could both be complex-valued, which may not correspond to any physical observables that can be measured experimentally. Furthermore, the choice of $h_{d+1}(\mathbf{k})$ is somewhat ambiguous. This also makes it hard to identify BISs precisely in experiments following this definition.

In the meantime, Ref. [87] also proposes a dynamical definition of BISs in their Eq. (4). It states that the BISs are formed by the collection of quasimomenta, at which the dynamical average of spin polarization $\overline{\langle \gamma_i(\mathbf{k}) \rangle} = \lim_{\tau \rightarrow \infty} \frac{1}{\tau} \int_0^\tau dt \langle \psi(\mathbf{k}, t) | \gamma_i | \psi(\mathbf{k}, t) \rangle$ vanishes for every spin component $i = 1, 2, \dots, d+1$, where $|\psi(\mathbf{k}, t)\rangle$ is the state of the sys-

tem evolved from a topologically trivial ground state $|\psi(\mathbf{k}, 0)\rangle$ (e.g., the lowest eigenstate of one spin component γ_i) prepared at time $t = 0$ to a later time t . This definition characterizes BISs by the vanishing of a real-valued spin texture $\overline{\langle \gamma_i(\mathbf{k}) \rangle}$, regardless of whether the evolution is unitary or not.

The behaviors of spin textures on the BISs can be further linked to topological properties of the system through the variation of time-averaged spin textures across the BISs. Considering a system prepared initially at a trivial phase, which is described by the ground state of some Hamiltonian $H_0(\mathbf{k})$. At time $t = 0$, a sudden quench is applied to the system, such that its dynamical evolution at any time $t > 0$ following the quench is governed by a Hamiltonian $H(\mathbf{k}) = \sum_{i=1}^{d+1} h_i(\mathbf{k}) \gamma_i$ with a topologically nontrivial ground state.

As an example, for a one dimensional system described by a chiral symmetric post-quench Hamiltonian $H(k) = h_x(k)\sigma_x + h_y(k)\sigma_y$, the BISs are formed by quasimomenta $k \in [-\pi, \pi]$ at which

$$\overline{\langle \sigma_j(k) \rangle} = \lim_{\tau \rightarrow \infty} \frac{1}{\tau} \int_0^\tau dt \langle \psi(k, t) | \sigma_j | \psi(k, t) \rangle = 0, \quad j = x, y. \quad (19)$$

Here $|\psi(k, t)\rangle$ is the state of the system evolved to time t following the quench. Qualitatively, the averaged spin textures $(\overline{\langle \sigma_x(k) \rangle}, \overline{\langle \sigma_y(k) \rangle})$ can vary across each BIS in three possible manners: (i) neither $\overline{\langle \sigma_x(k) \rangle}$ nor $\overline{\langle \sigma_y(k) \rangle}$ changes sign; (ii) both $\overline{\langle \sigma_x(k) \rangle}$ and $\overline{\langle \sigma_y(k) \rangle}$ change signs; (iii) only one component in $\overline{\langle \sigma_x(k) \rangle}$ and $\overline{\langle \sigma_y(k) \rangle}$ changes sign.

To relate the spin textures to the topological property of the post-quench Hamiltonian $H(\mathbf{k})$, Ref. [87] introduced a dynamical spin texture field $\mathbf{g}(\mathbf{k})$, whose components are given by $g_i(\mathbf{k}) \equiv -\frac{1}{N_{\mathbf{k}}} \partial_{k_\perp} \gamma_i(\mathbf{k})$, with $N_{\mathbf{k}}$ being the normalization factor and k_\perp being the quasimomentum perpendicular to the BIS. A topological winding number $w_{d-1} = \sum_j \frac{\Gamma(d/2)}{2\pi^{d/2}} \frac{1}{(d-1)!} \int_{\text{BIS}_j} \mathbf{g}(\mathbf{k}) [d\mathbf{g}(\mathbf{k})]^{d-1}$ of the dynamical spin texture field $\mathbf{g}(\mathbf{k})$ on the BISs was introduced, and proved to be equal to the topological invariant ν_d characterizing the ground state of the post-quench Hamiltonian $H(\mathbf{k})$ [87], i.e.,

$$\nu_d = w_{d-1}. \quad (20)$$

The formalism proposed in Ref. [87] is applicable to both closed and open quantum systems. Therefore, it should also be useful to extract the topological invariants of a non-Hermitian system in its non-unitary dynamics. To do this, we introduce the stroboscopic time-averaged spin textures of our PDNHL model as

$$\overline{\langle \sigma_j(k) \rangle}_\alpha \equiv \lim_{M \rightarrow \infty} \frac{1}{M} \sum_{m=1}^M \langle \sigma_j(k, m) \rangle_\alpha, \quad j = x, y. \quad (21)$$

The stroboscopic spin expectation value $\langle \sigma_j(k, m) \rangle_\alpha$ is given by

$$\langle \sigma_j(k, m) \rangle_\alpha = \frac{\langle \phi_0 | [U_\alpha^\dagger(k)]^m \sigma_j U_\alpha^m(k) | \phi_0 \rangle}{\langle \phi_0 | [U_\alpha^\dagger(k)]^m U_\alpha^m(k) | \phi_0 \rangle}, \quad \alpha = 1, 2. \quad (22)$$

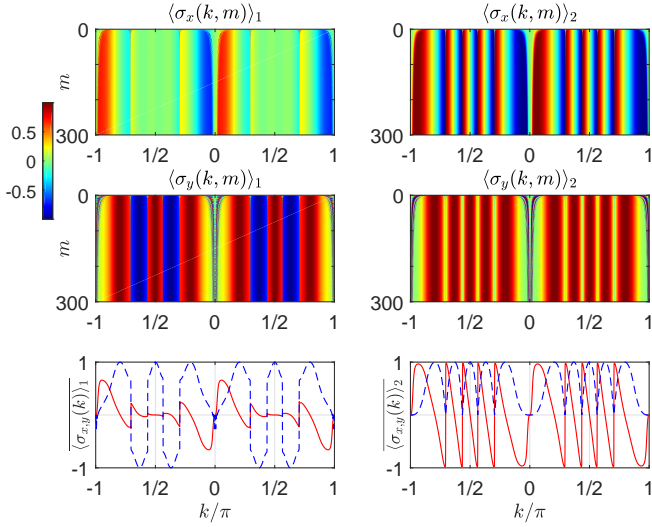


FIG. 9. Stroboscopic spin expectation values $\langle \sigma_j(k, m) \rangle_\alpha$ (top and middle panels) and stroboscopic time-averaged spin textures $\langle \sigma_j(k) \rangle_\alpha$ (bottom panels) versus the quasimomentum k for spin components $j = x, y$ in time frames $\alpha = 1, 2$. System parameters are chosen as $\mu = 0$, $r_x = \frac{5\pi}{2}$, $r_y = \frac{\pi}{2}$, and $\gamma = \text{arccosh}(\sqrt{2})$. In bottom panels, results for $\langle \sigma_x(k) \rangle_{1,2}$ (red solid lines) and $\langle \sigma_y(k) \rangle_{1,2}$ (blue dashed lines) at each k are obtained after averaging over 300 driving periods.

Here $|\phi_0\rangle$ is the initial state, and $U_\alpha(k)$ is the Floquet operator in symmetric time frame α as defined by Eqs. (8) and (9). The normalization factor $\langle \phi_0 | [U_\alpha^\dagger(k)]^m U_\alpha^m(k) | \phi_0 \rangle$ is introduced since the dynamics is not unitary. Note that the Pauli matrices here acting on spins instead of sublattice degrees of freedom. In cold atom systems, these degrees of freedom correspond to internal states of atoms, such as the ground hyperfine levels $5^2S_{1/2}F = 1$ and $5^2S_{1/2}F = 2$ of ^{87}Rb [36].

To image the bulk topological invariant of our PDNHL model, we consider dynamics following a sudden quench at the initial time $t = 0$ from the prequench Hamiltonian $h_0(k) = \sigma_z$ to the postquench Hamiltonian $h_\alpha(k) = i \ln U_\alpha(k)$, executed separately in the two symmetric time frames $\alpha = 1, 2$. The initial states in all cases are chosen to be the ground states of $h_0(k)$ at all $k \in [-\pi, \pi)$, and the spin textures in postquench dynamics are obtained numerically from Eqs. (21) and (22).

Computation examples of $\langle \sigma_j(k, m) \rangle_\alpha$ and $\langle \sigma_j(k) \rangle_\alpha$ for two hopping amplitudes $r_x = \frac{\pi}{2}$ and $\frac{5\pi}{2}$, with other system parameters fixed at $\mu = 0$, $r_y = \frac{\pi}{2}$ and $\gamma = \text{arccosh}(\sqrt{2})$ are presented in Figs. 8 and 9. The results for all $\langle \sigma_j(k) \rangle_\alpha$ are averaged over $M = 300$ driving periods.

The dynamical spin texture field of our model in time frame α contains two components $g_x^\alpha(k) = -\frac{1}{N_k} \partial_{k_\perp} \langle \sigma_x(k) \rangle_\alpha$ and $g_y^\alpha(k) = -\frac{1}{N_k} \partial_{k_\perp} \langle \sigma_y(k) \rangle_\alpha$, where the normalization factor $N_k = \sqrt{(\partial_{k_\perp} \langle \sigma_x(k) \rangle_\alpha)^2 + (\partial_{k_\perp} \langle \sigma_y(k) \rangle_\alpha)^2}$. From the numerical results presented in bottom panels of Figs. 8 and 9, we notice that all BISs are extremum points of $\langle \sigma_y(k) \rangle_\alpha$. So $g_y^\alpha(k) = 0$ on the BISs, and we only need to consider the behavior of $g_x^\alpha(k)$ there, which has the form $[g_x^\alpha(k)]_j = [-\text{sgn}(\partial_{k_\perp} \langle \sigma_x(k) \rangle_\alpha)]_j$ at

the j th BIS. The corresponding topological winding number

$$w_0^\alpha = \sum_j \frac{1}{2} [-\text{sgn}(\partial_{k_\perp} \langle \sigma_x(k) \rangle_\alpha)]_j, \quad (23)$$

will be quantized if the BISs come in pairs. Then according to the general relation (20), the two winding numbers w_0^1 and w_0^2 should be related to the topological invariants in the two symmetric time frames W_1 and W_2 [see Eq. (16)]:

$$W_1 = w_0^1, \quad W_2 = w_0^2. \quad (24)$$

We can now extract the topological invariants of our PDNHL system from the bottom panels of Figs. 8 and 9 with the help of Eqs. (23) and (24).

In the bottom panels of Fig. 8, assuming k_\perp points to left, we have $\text{sgn}(\partial_{k_\perp} \langle \sigma_x(k) \rangle_\alpha) = -1$ at the two BISs $k = 0, \pi$ in both time frames $\alpha = 1, 2$. Eqs. (23) and (24) then yield $W_1 = w_0^1 = 1$ and $W_2 = w_0^2 = 1$, which are the same as the W_1 and W_2 calculated by Eq. (16). Using Eq. (17), the two topological invariants W_0, W_π of our system are given by $W_0 = (w_0^1 + w_0^2)/2 = 1$ and $W_\pi = (w_0^1 - w_0^2)/2 = 0$, which are consistent with the results shown in the phase diagram Fig. 5.

In the bottom panels of Fig. 9, we have $\text{sgn}(\partial_{k_\perp} \langle \sigma_x(k) \rangle_\alpha) = -1$ at all BISs in both time frames $\alpha = 1, 2$. Notably, there is one pair of BISs for spin textures in time frame 1 (bottom left panel of Fig. 9) and five pairs of BISs for spin textures in time frame 2 (bottom right panel of Fig. 9). Eqs. (23) and (24) then yield $W_1 = w_0^1 = 1$ and $W_2 = w_0^2 = 5$, which are the same as the W_1 and W_2 calculated by Eq. (16). Using Eq. (17), the two topological invariants W_0, W_π of our system are given by $W_0 = (w_0^1 + w_0^2)/2 = 3$ and $W_\pi = (w_0^1 - w_0^2)/2 = -2$, which are also consistent with the results shown in the phase diagram Fig. 5.

For system parameters sitting in regular regions of the phase diagram [i.e., $(r_x, r_y) \in (0, \pi - \arccos(1/\cosh \gamma)) \times (0, \infty)$ and $(r_x, r_y) \in (0, \infty) \times (0, \pi)$], we have checked and found the consistency between the winding numbers extracted from the time-averaged spin textures $\langle \sigma_{x,y}(k) \rangle_{1,2}$ and those obtained theoretically from Eq. (16). Therefore we conclude that the time-averaged spin textures, proposed first in Ref. [87], can also be a useful tool to image the bulk invariants of non-Hermitian Floquet topological phases. Experimentally, the measurement of these spin textures is already available in cold atom systems [86], providing direct signatures of topological invariants from bulk state dynamics as complementary to the detection of edge states.

In experiments, the existence of noise and mesoscopic fluctuations may challenge the resolution of spin textures in long-time domains. In Ref. [87], the spin textures averaged over a long time have been shown to be robust to slow decay rates. With stronger dissipation effects, our numerical results presented in Figs. 8 and 9 suggesting that the spin textures converge quickly to stable patterns within the initial tenth of periods. The topological signatures of our model may then be extracted from the spin textures within a relatively short evolution time, in which the effect of noise may not be fully developed. Indeed, in a recent realization of non-Hermitian pho-

tonic quantum walks, spin textures related to the topological properties of the system have also been successfully imaged in a relatively short evolution time [88].

More generally, it is interesting to know whether the time averaged spin textures studied here can also be used to image the topological invariants of other non-Hermitian systems in different symmetry classes and at different physical dimensions. These questions are beyond the scope of this manuscript and we will leave it for future explorations.

VI. SUMMARY AND DISCUSSION

In this work, we explored Floquet topological phases in a periodically driven non-Hermitian lattice model. We found the bulk phase diagram of the system analytically, with phase boundaries formed by Floquet BTPs of complex quasienergies versus system parameters. Each of the phases in the diagram is characterized by a pair of topological winding numbers, which take integer values and predict the number of topological edge states at 0 and π -quasienergies of the Floquet spectrum. Along certain regular directions of the phase diagram, we also found Floquet topological phases with unlimited winding numbers and arbitrarily many *real*-quasienergy edge states induced solely by the non-Hermiticity of the system. These edge states are also robust to (non-)Hermitian perturbations which do not break the chiral symmetry of the system. We further suggested a dynamical approach to extract the bulk topological winding numbers of the system by investigating its stroboscopic spin textures [87]. A simple connection was observed between the number of times of spin flips over the Brillouin zone in long time limit and the winding numbers, suggesting a promising route to detect these non-Hermitian Floquet topological phases in cold atom systems or other quantum simulators.

Around spectral singularities, noise and mesoscopic fluctuations could have pronounced effects, which may blur the boundary between different topological phases of our model. However, as shown in our phase diagram Fig. 5, many non-Hermitian Floquet topological phases of our model can be found in wide parameter windows. Deep into each of these parameter window, the topological edge states are well gapped from other bulk states in the corresponding phase. The existence of spectral gaps could then provide protections to the found edge states against noise effects. Experimentally, topological edge states have been observed in non-Hermitian systems [89], which also motivate us to ignore the effect of noise in the current study.

By setting $\mu \neq 0$ in the model considered in this manuscript, more asymmetry could appear in its phase diagram, resulting in other possible non-Hermitian Floquet topological phases. A thorough exploration of these situations will be left for future study. An extension of the model studied here to two-dimension may also allow the appearance of anomalous chiral edge states traversing both the 0- and π -quasienergy gaps of the Floquet spectrum. The topological characterization of these non-Hermitian anomalous edge states in Floquet systems and their possible bulk-edge correspondence are also in-

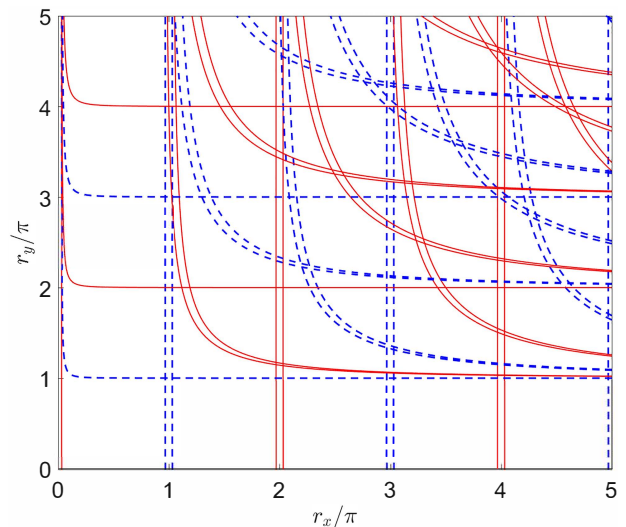


FIG. 10. Phase boundary diagram of the PDNHL model in the parameter space $(r_x, r_y) \in (0, 5\pi] \times (0, 5\pi]$, with other system parameters fixed at $\mu = 0$ and $\gamma = 0.1$. Trajectories of Floquet BTPs corresponding to spectrum gap closings at quasienergy zero (π) are denoted by red solid (blue dashed) lines.

teresting topics for future explorations.

ACKNOWLEDGEMENT

J.G. is supported by the Singapore NRF grant No. NRF-NRFI2017-04 (WBS No. R-144-000-378-281) and the Singapore Ministry of Education Academic Research Fund Tier I (WBS No. R-144-000-353-112).

Appendix A: Phase boundary diagram: more examples

In this appendix, we give two more examples of the phase boundary diagrams formed by the trajectories of Floquet BTPs in the r_x - r_y parameter space. The other system parameters are chosen as $\mu = 0$, $\gamma = 0.1$ and $\mu = 0$, $\gamma = 5$ for the two examples presented here. All the results are obtained from Eq. (7) in the main text.

In the first example as shown in Fig. 10, the system is close to its Hermitian limit, with a small non-Hermitian coupling $\gamma = 0.1$. Compared with the phase diagram of the corresponding Hermitian Floquet system (see Fig. 1 of Ref. [36]), each phase boundaries now splits into a pair of closely spaced trajectories formed by Floquet BTPs. In between, new Floquet topological phases induced by non-Hermiticity appear, as discussed in the main text. But major parts of the phase diagram are still dominated by Floquet topological phases carried over from the system in its Hermitian limit.

In the second example as shown in Fig. 11, the system is close to a non-Hermitian limit with a relatively large non-Hermitian coupling $\gamma = 5$. New phase boundaries generated

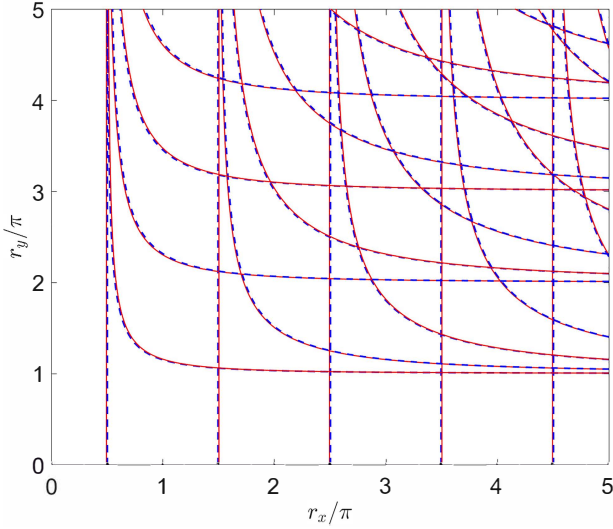


FIG. 11. Phase boundary diagram of the PDNHL model in the parameter space $(r_x, r_y) \in (0, 5\pi] \times (0, 5\pi]$, with other system parameters fixed at $\mu = 0$ and $\gamma = 5$. Trajectories of Floquet BTPs corresponding to spectrum gap closings at quasienergy zero (π) are denoted by red solid (blue dashed) lines.

by non-Hermitian effects are now shifted in a way, such that each trajectory of Floquet BTPs related to a gap closing at quasienergy zero is almost overlapped with another trajectory of Floquet BTPs related to a gap closing at quasienergy π . This means that crossing these phase boundaries from one side to the other, we will encounter phase transitions accompanied by spectrum gap closings at both zero and π quasienergies simultaneously, which is very different from the situations of the system in its Hermitian limit. Therefore, a large non-Hermitian coupling γ could introduce strong modifications to the topological phases of our PDNHL model.

Appendix B: Floquet spectrum and edge states under open boundary conditions: more examples

In this appendix, we present more examples of the Floquet spectrum of the PDNHL model under OBC.

In Fig. 12, we presented the Floquet spectrum E versus hopping amplitude r_y at fixed values of hopping amplitude $r_x = \frac{\pi}{2}$ and non-Hermitian coupling strength $\gamma = \text{arccosh}(\sqrt{2})$ in a lattice of $N = 300$ unit cells. In Fig. 12(c), the red solid and blue dashed lines correspond to phase boundaries obtained from the Eq. (7) for Floquet BTPs. We see that the number of edge state pairs (n_0, n_π) , as denoted in Fig. 12(c), changes across each of the phase boundaries. Furthermore, refer to Fig. 3, we find that (n_0, n_π) matches exactly the absolute value of winding number $(|W_0|, |W_\pi|)$ in each of the corresponding non-Hermitian Floquet topological phases. Therefore the relation (18) is verified for the example considered here. In Fig. 13, we further showed the quasienergy spectrum at $r_x = \frac{\pi}{2}$, $\gamma = \text{arccosh}(\sqrt{2})$ with $r_y = \pi, 2\pi, 3\pi$ and 4π in the complex quasienergy plane. In all these examples, we see that

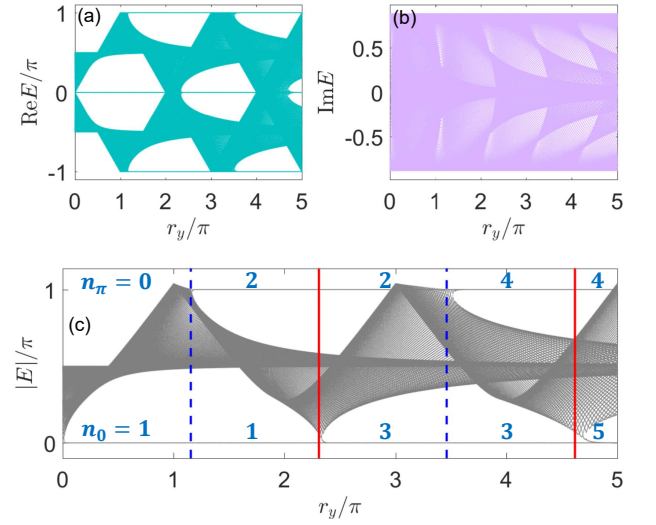


FIG. 12. The Floquet spectrum of \hat{U} versus hopping amplitude r_y under OBC. The lattice has $N = 300$ unit cells. Other system parameters are fixed at $\mu = 0$, $r_x = \frac{\pi}{2}$ and $\gamma = \text{arccosh}(\sqrt{2})$. Panels (a) and (b) show the real and imaginary parts of the quasienergy E . Panel (c) shows the absolute values of quasienergy E . Red solid (blue dashed) lines represent phase boundaries at which the spectrum gaps close at quasienergy zero (π). They are obtained from Eq. (7) in the main text for Floquet BTPs. The integers in light blue in panel (c) denote the number of degenerate edge state pairs at quasienergies zero (n_0) and π (n_π). Their values are equal to the absolute values of winding numbers W_0 and W_π as shown in Fig. 3(b) of the main text, respectively.

edge states at $E = 0$ and $\pm\pi$ have real quasienergies and are surrounded by gaps in the complex quasienergy plane.

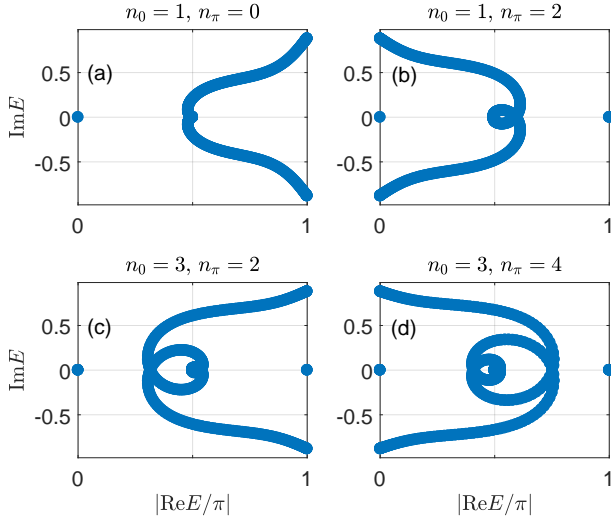


FIG. 13. The Floquet spectrum of \hat{U} at separate values of r_y shown in the complex quasienergy plane. The lattice has $N = 300$ unit cells. Other system parameters are fixed at $\mu = 0$, $r_x = \frac{\pi}{2}$ and $\gamma = \text{arccosh}(\sqrt{2})$. Dots at $\text{Im}E = 0$ and $|\text{Re}E| = 0$ ($|\text{Re}E| = \pi$) represent degenerate edge states with real quasienergy zero (π). Other dots denote bulk states with complex quasienergies. Panel (a): $r_y = \pi$, there is one pair of edge states at quasienergy $E = 0$, and no edge states at quasienergy $E = \pi$. Panel (b): $r_y = 2\pi$, there is one pair of edge states at quasienergy $E = 0$, and two pairs of edge states at quasienergy $E = \pi$. Panel (c): $r_y = 3\pi$, there is three pairs of edge states at quasienergy $E = 0$, and two pairs of edge states at quasienergy $E = \pi$. Panel (d): $r_y = 4\pi$, there are three pairs of edge states at quasienergy $E = 0$, and four pairs of edge states at quasienergy $E = \pi$.

-
- [1] T. Oka and H. Aoki, Phys. Rev. B **79**, 081406 (2009).
[2] N. H. Lindner, G. Refael, and V. Galitski, Nat. Phys. **7**, 490 (2011).
[3] J. P. Dahlhaus, J. M. Edge, J. Tworzydło, and C. W. J. Beenakker, Phys. Rev. B **84**, 115133 (2011).
[4] T. Kitagawa, T. Oka, A. Brataas, L. Fu, and E. Demler, Phys. Rev. B **84**, 235108 (2011).
[5] H. Wang, D. Y. H. Ho, W. Lawton, J. Wang, and J. Gong, Phys. Rev. E **88**, 052920 (2013).
[6] D. Y. H. Ho and J. Gong, Phys. Rev. Lett. **109**, 010601 (2012).
[7] Q.-J. Tong, J.-H. An, J. Gong, H.-G. Luo, and C. H. Oh, Phys. Rev. B **87**, 201109 (2013).
[8] L. Zhou, H. Wang, D. Y. H. Ho, and J. Gong, Eur. Phys. J. B **87**, 204 (2014).
[9] T.-S. Xiong, J. Gong, and J.-H. An, Phys. Rev. B **93**, 184306 (2016).
[10] Á. Gómez-León and G. Platero, Phys. Rev. Lett. **110**, 200403 (2013).
[11] J. Cayssol, B. Dóra, F. Simon, and R. Moessner, Phys. Status Solidi Rapid Res. Lett. **7**, 101 (2013).
[12] M. Thakurathi, A. A. Patel, D. Sen and A. Dutta, Phys. Rev. B **88**, 155133 (2013).
[13] A. G. Grushin, Á. Gómez-León, and T. Neupert, Phys. Rev. Lett. **112**, 156801 (2014).
[14] R. Wang, B. Wang, R. Shen, L. Sheng, and D. Y. Xing, Europhys. Lett. **105**, 17004 (2014).
[15] P. Titum, N. H. Lindner, M. C. Rechtsman, and G. Refael, Phys. Rev. Lett. **114**, 056801 (2015).
[16] J. Klinovaja, P. Stano, and D. Loss, Phys. Rev. Lett. **116**, 176401 (2016); M. Thakurathi, D. Loss, and J. Klinovaja, Phys. Rev. B **95**, 155407 (2017).
[17] Y. Chen and C. Tian, Phys. Rev. Lett. **113**, 216802 (2014); C. Tian, Y. Chen, and J. Wang, Phys. Rev. B **93**, 075403 (2016).
[18] T. Kitagawa, E. Berg, M. Rudner, and E. Demler, Phys. Rev. B **82**, 235114 (2010).
[19] L. Jiang, T. Kitagawa, J. Alicea, A. R. Akhmerov, D. Pekker, G. Refael, J. I. Cirac, E. Demler, M. D. Lukin, and P. Zoller, Phys. Rev. Lett. **106**, 220402 (2011).
[20] A. Kundu and B. Seradjeh, Phys. Rev. Lett. **111**, 136402 (2013).
[21] R. W. Bomantara, G. N. Raghava, L. Zhou, and J. Gong, Phys. Rev. E **93**, 022209 (2016); R. W. Bomantara and J. Gong, Phys. Rev. B **94**, 235447 (2016).
[22] M. Lababidi, I. I. Satija, and E. Zhao, Phys. Rev. Lett. **112**, 026805 (2014); Z. Zhou, I. I. Satija, and E. Zhao, Phys. Rev. B **90**, 205108 (2014).
[23] M. D. Reichl and E. J. Mueller, Phys. Rev. A **89**, 063628 (2014).

- [24] Á. Gómez-León, P. Delplace, and G. Platero, Phys. Rev. B **89**, 205408 (2014).
- [25] M. S. Rudner, N. H. Lindner, E. Berg, and M. Levin, Phys. Rev. X **3**, 031005 (2013); P. Titum, E. Berg, M. S. Rudner, G. Refael, and N. H. Lindner, Phys. Rev. X **6**, 021013 (2016).
- [26] I. C. Fulga and M. Maksymenko, Phys. Rev. B **93**, 075405 (2016).
- [27] L. Zhou, C. Chen, and J. Gong, Phys. Rev. B **94**, 075443 (2016).
- [28] J. K. Asbóth, Phys. Rev. B **86**, 195414 (2012). J. K. Asbóth, and H. Obuse, Phys. Rev. B **88**, 121406 (2013).
- [29] F. Nathan and M. S. Rudner, New J. Phys. **17**, 125014 (2015).
- [30] R. Roy and F. Harper, Phys. Rev. B **94**, 125105 (2016); R. Roy and F. Harper, Phys. Rev. B **96**, 155118 (2017).
- [31] S. Yao, Z. Yan, and Z. Wang, Phys. Rev. B **96**, 195303 (2017).
- [32] M. Rodríguez-Vega and B. Seradjeh, Phys. Rev. Lett. **121**, 036402 (2018).
- [33] H. H. Yap, L. Zhou, J. Wang, and J. Gong, Phys. Rev. B **96**, 165443 (2017).
- [34] H. H. Yap, L. Zhou, C. H. Lee, J. Gong, Phys. Rev. B **97**, 165142 (2018).
- [35] D. Y. H. Ho and J. Gong, Phys. Rev. B **90**, 195419 (2014).
- [36] L. Zhou and J. Gong, Phys. Rev. A **97**, 063603 (2018).
- [37] L. Zhou and J. Gong, Phys. Rev. B **97**, 245430 (2018).
- [38] L. Li, C. H. Lee, and J. Gong, Phys. Rev. Lett. **121**, 036401 (2018).
- [39] G. Jotzu, M. Messer, R. Desbuquois, M. Lebrat, T. Uehlinger, D. Greif, and T. Esslinger, Nature **515**, 237 (2014); M. Aidelsburger, M. Lohse, C. Schweizer, M. Atala, J. T. Barreiro, S. Nascimbène, N. R. Cooper, I. Bloch and N. Goldman, Nat. Phys. **11**, 162 (2015).
- [40] N. Fläschner, B. S. Rem, M. Tarnowski, Vogel, D.-S. Lühmann, K. Sengstock, and C. Weitenberg, Science **352**, 1091 (2016).
- [41] T. Kitagawa, M. A. Broome, A. Fedrizzi, M. S. Rudner, E. Berg, I. Kassal, A. Aspuru-Guzik, E. Demler and A. G. White, Nat. Commun. **3**, 882 (2012).
- [42] M. C. Rechtsman, J. M. Zeuner, Y. Plotnik, Y. Lumer, D. Podolsky, F. Dreisow, S. Nolte, M. Segev, and A. Szameit, Nature **496**, 196 (2013); W. Hu, J. C. Pillay, K. Wu, M. Pasek, P. P. Shum, and Y. D. Chong, Phys. Rev. X **5**, 011012 (2015).
- [43] L. J. Maczewsky, J. M. Zeuner, S. Nolte, and A. Szameit, Nat. Commun. **8**, 13756 (2017); S. Mukherjee, A. Spracklen, M. Valiente, E. Andersson, P. Ohberg, N. Goldman, and R. R. Thomson, Nat. Commun. **8**, 13918 (2017).
- [44] M. Xiao, G. Ma, Z. Yang, P. Sheng, Z. Q. Zhang, and C. T. Chan, Nat. Phys. **11**, 240 (2015); R. Süsstrunk and S. D. Huber, Science **349**, 47 (2015); R. Fleury, A. B. Khanikaev and A. Alù, Nat. Commun. **7**, 11744 (2016); R. Süsstrunk, P. Zimmermann, and S. D. Huber, New J. Phys. **19**, 015013 (2017).
- [45] Y. Peng, C. Qin, D. Zhao, Y. Shen, X. Xu, M. Bao, H. Jia, and X. Zhu, Nat. Commun. **7**, 13368 (2016).
- [46] V. M. M. Alvarez, J. E. B. Vargas, M. Berdakin, and L. E. F. Foa Torres, arXiv:1805.08200 (2018).
- [47] C. Yuce, The European Physical Journal D **69**, 184 (2015); Z. Turker, S. Tombuloglub, and C. Yuce, Phys. Lett. A **382**, 2013 (2018).
- [48] D. Kim, M. Ken, N. Kawakami, H. Obuse, arXiv:1609.09650 (2016).
- [49] J. Gong and Q. Wang, Phys. Rev. A **91**, 042135 (2015).
- [50] C. Dembowski, H.-D. Gräf, H. L. Harney, A. Heine, W. D. Heiss, H. Rehfeld, and A. Richter, Phys. Rev. Lett. **86**, 787 (2001).
- [51] R. Uzdin, A. Mailybaev, and N. Moiseyev, J. Phys. A **44**, 435302 (2011).
- [52] M. V. Berry and R. Uzdin, J. Phys. A **44**, 435303 (2011).
- [53] W. D. Heiss, J. Phys. A: Math. Theor. **45**, 444016 (2012).
- [54] W. Hu, H. Wang, P. P. Shum, and Y. D. Chong, Phys. Rev. B **95**, 184306 (2017).
- [55] D. Halpern, H. Li, and T. Kottos, Phys. Rev. A **97**, 042119 (2018).
- [56] J. Gong and Q. Wang, Phys. Rev. A **97**, 052126 (2018).
- [57] H. Zhou, C. Peng, Y. Yoon, C. W. Hsu, K. A. Nelson, L. Fu, J. D. Joannopoulos, M. Soljačić, and B. Zhen, Science **359**, 1009 (2018).
- [58] M. S. Rudner and L. S. Levitov, Phys. Rev. Lett. **102**, 65703 (2009).
- [59] J. M. Zeuner, M. C. Rechtsman, Y. Plotnik, Y. Lumer, S. Nolte, M. S. Rudner, M. Segev, and A. Szameit, Phys. Rev. Lett. **115**, 40402 (2015).
- [60] K. Mochizuki, D. Kim, and H. Obuse, Phys. Rev. A **93**, 062116 (2016).
- [61] Y. Huang, Z. Yin, and W. L. Yang, Phys. Rev. A **94**, 022302 (2016).
- [62] T. Rakovszky, J. K. Asbóth, and A. Alberti, Phys. Rev. B **95**, 201407 (2017).
- [63] L. Xiao, X. Zhan, Z. H. Bian, K. K. Wang, X. Zhang, X. P. Wang, J. Li, K. Mochizuki, D. Kim, N. Kawakami, W. Yi, H. Obuse, B. C. Sanders, and P. Xue, Nat. Phys. **13**, 1117 (2017); L. Xiao, X. Qiu, K. Wang, Z. Bian, X. Zhan, H. Obuse, B. C. Sanders, W. Yi, and P. Xue, arXiv:1810.00594 (2018).
- [64] T. Chen, B. Wang, and X. Zhang, Phys. Rev. A **97**, 052117 (2018).
- [65] A. K. Harter, A. Saxena, and Y. N. Joglekar, Sci. Rep. **8**, 12065 (2018).
- [66] K. Wang, X. Qiu, L. Xiao, X. Zhan, Z. Bian, W. Yi, and P. Xue, arXiv:1806.10871 (2018).
- [67] S. Malzard, C. Poli, and H. Schomerus, Phys. Rev. Lett. **115**, 200402 (2015).
- [68] Y. Xu, S. Wang, and L.-M. Duan, Phys. Rev. Lett. **118**, 045701 (2017).
- [69] T.E. Lee, Phys. Rev. Lett. **116**, 133903 (2016).
- [70] S. Weimann, M. Kremer, Y. Plotnik, Y. Lumer, S. Nolte, K.G. Makris, M. Segev, M.C. Rechtsman, A. Szameit, Nat. Mater. **16**, 433 (2017).
- [71] D. Leykam, K. Y. Bliokh, C. Huang, Y. Chong, F. Nori, Phys. Rev. Lett. **118**, 040401 (2017).
- [72] L. Zhou, Q.h. Wang, H. Wang, J. Gong, Phys. Rev. A **98**, 022129 (2018).
- [73] H. Shen, B. Zhen, L. Fu, Phys. Rev. Lett. **120**, 146402 (2018).
- [74] C. Yin, H. Jiang, L. Li, R. Lu, S. Chen, Phys. Rev. A **97**, 052115 (2018).
- [75] J.W. Ryu, N. Myoung, H.C. Park, Phys. Rev. B **96**, 125421 (2017); J. W. Ryu, N. Myoung, H. C. Park, Sci. Rep. **7**, 8746 (2017).
- [76] C. Yuce, Phys. Rev. A **97**, 042118 (2018).
- [77] S. Yao, Z. Wang, Phys. Rev. Lett. **121**, 086803 (2018).
- [78] S. Lieu, Phys. Rev. B **97**, 045106 (2018).
- [79] To see this, one can Taylor expand $e^{-ih_x(k)\sigma_x} = \cos[h_x(k)] - i \sin[h_x(k)]\sigma_x$ and $e^{-i[h_y(k)+i\gamma]\sigma_y} = \cos[h_y(k) + i\gamma] - i \sin[h_y(k) + i\gamma]\sigma_y$, multiplying these two terms and rewriting them into the form $e^{-iH(k)}$ with the help of the Euler formula. Here the Floquet effective Hamiltonian $H(k) = E(k)\hat{\mathbf{n}}(k) \cdot \sigma$, with $\hat{\mathbf{n}}(k)$ being a unit vector and $\sigma = (\sigma_x, \sigma_y, \sigma_z)$. Then $H(k)$ has two bands with quasienergy dispersions $\pm E(k)$.
- [80] Y. C. Hu, T. L. Hughes, Phys. Rev. B **84**, 153101 (2011).
- [81] K. Esaki, M. Sato, K. Hasebe, M. Kohmoto, Phys. Rev. B **84**, 205128 (2011).
- [82] Y. Xiong, Journal of Physics Communications **2**, 035043 (2018).

- [83] V. M. Martinez Alvarez, J. E. Barrios Vargas, and L. E. F. Foa Torres, *Phys. Rev. B* **97**, 121401 (2018).
- [84] Z. Gong, Y. Ashida, K. Kawabata, K. Takasan, S. Higashikawa, M. Ueda, *Phys. Rev. X* **8**, 031079 (2018).
- [85] F. K. Kunst, E. Edvardsson, J. C. Budich, and E. J. Bergholtz, *Phys. Rev. Lett.* **121**, 026808 (2018).
- [86] W. Sun, C. Yi, B. Wang, W. Zhang, B. C. Sanders, X. Xu, Z. Wang, J. Schmiedmayer, Y. Deng, X. Liu, S. Chen, and J. Pan, *arXiv:1804.08226* (2018).
- [87] L. Zhang, L. Zhang, S. Niu, and X. Liu, *arXiv:1802.10061* (2018).
- [88] K. Wang, X. Qiu, L. Xiao, X. Zhan, Z. Bian, B. C. Sanders, W. Yi, and P. Xue, *arXiv:1808.06446* (2018).
- [89] W. Zhu, X. Fang, D. Li, Y. Sun, Y. Li, Y. Jing, and H. Chen, *Phys. Rev. Lett.* **121**, 124501 (2018).